JOURNAL OF COMPUTATIONAL PHYSICS 17, 192–208 (1975)

Fluid Simulation of a Low-Pressure Axisymmetric Toroidal Plasma Using Natural Coordinates

R. C. GRIMM AND J. L. JOHNSON*

Plasma Physics Laboratory, Princeton University, Princeton, New Jersey 08540

Received June 21, 1974; revised October 22, 1974

A numerical model is developed to study the confinement of low-pressure plasmas in axially symmetric configurations with arbitrary shaped magnetic surfaces. The equations contain the effects of resistivity, plasma inertia, and pressure gradients in the surfaces. In this model, which extends the earlier work in which fictitious currents had to be introduced to support the magnetic fields, the plasma pressure is taken sufficiently small that only electrostatic modes can be excited. The Lax–Wendroff scheme is used to advance the plasma density and velocities in time. Applications include demonstration that classical expressions for diffusion are valid when there are small plasma flows, and study of the propagation of acoustic and geodesic waves in levitrons.

I. INTRODUCTION

Following the nonlinear time developement of plasma motion in realistic geometries can provide considerable understanding of toroidal confinement. The time behavior of most plasma physics experiments is a complex combination of different motions, usually complicated by very different time scales, nonlinear effects and nontrivial boundary conditions. Numerical calculations can play a very important role in the study of phenomena of this kind; they enable a direct comparison of the different physical effects, provide a practical means of comparing theory with experiment, and quite often suggest realistic simplifications to the theory which make it amenable to analysis.

From a computational point of view, the presence of physical phenomena on different time scales makes selecting an appropriate numerical scheme which provides suitable accuracy and convergence properties difficult. Typically one constructs models from the full set of equations which display effects on some particular time scale, and pieces together a more complete physical picture of the experiment from these models. Motions on very short time scales (using particle codes) and on long time scales (adopting transport equations) have received

* On loan from Westinghouse Research Laboratories.

considerable attention, and reliable numerical techniques for their study are well known in the literature. Description of motions on intermediate time scales can also be studied with transport or fluid codes. Several difficulties must be faced; realistic descriptions are invariably two (or more) dimensional in nature, the choice of model is strongly dependent on the time scale of the phenomena of interest, and fluid models are not always easily justified. On the other hand, an understanding of motions on the different time scales is important (it may lead to modifications in the models appropriate for longer time scales for example), and the numerical calculations may give a sensible qualitative description even for experimental configurations where the model cannot be rigorously justified theoretically.

The numerical study of confinement on the thermal time scale in toroidal devices has received considerable attention in recent years. Winsor, Johnson and Dawson [1], using a simple one-fluid magnetohydrodynamic model, devised an appropriate method of solution for low-pressure devices and followed the development of an initial state in the minor cross section. They studied the onset of rotational buildup [2] and measured plasma diffusion across model circular magnetic surfaces. Good agreement was reported with extensive analytical solutions [3]. The model was subsequently improved to include finite gyration radius effects and Hall terms in Ohm's law [4]. The development of weak shocks was reported and confirmed analytically [5, 6]. The effects of viscosity and thermal conductivity towards the stabilization of the rotating flows has also been considered [7–11]. More recently the effect of rotational transform on shocked equilibria has been investigated [12]. Haines [13] considered toroidal confinement as an initial-value problem, ordering the equations to obtain a set of five coupled nonlinear time-dependent equations which were solved numerically.

Two major simplifications are common to these calculations. Most importantly, the plasma motion is assumed to be electrostatic so that the magnetic field does not change in time. Since this corresponds to ignoring the perturbation of the magnetic field in the equation of motion while properly retaining the change in the plasma current, the assumption is well justified in low-pressure systems. Indeed, for levitrons or model stellarators where the only current in the plasma is associated with material pressure, the neglected force associated with the $\mathbf{J} \times \mathbf{B}$ term in the momentum equation is of order β^2; in tokamaks where the poloidal field is maintained by current in the plasma, it is of order $\beta\epsilon$ with ϵ the inverse aspect ratio. The other major simplification is that the magnetic field, in which the magnetic surfaces have nested, concentric, circular cross sections, is not self-consistent and does not contain important physical effects associated with toroidally imposed shifts of the surfaces.

The numerical techniques developed previously [1] take advantage of the different nature of the equations in directions parallel and perpendicular to the field lines,

and rely heavily on the coincidence of coordinate surfaces and magnetic surfaces. In the present calculation this model is extended to apply to a general axisymmetric field geometry. This is achieved by performing the calculations in field line coordinates, in such a way that the grid points are actually determined to lie on magnetic surfaces. The model is applicable for low-pressure configurations where the electrostatic assumption can be justified.

In Section II we describe a simple one-fluid magnetohydrodynamic model which contains the effects of inertia, scalar pressure, electrical conductivity, and a static magnetic field. In Section III we derive expressions for the geometry used in the calculations. The finite-difference scheme is described in Section IV. Section V is devoted to a discussion of boundary and initial conditions. Some preliminary applications are discussed in Section VI.

II. Physical Model

We consider a simple, scalar pressure fluid described by the equations

$$(\partial\rho/\partial t) + \nabla \cdot \rho\mathbf{v} = 0, \tag{1}$$

$$\rho((\partial\mathbf{v}/\partial t) + \mathbf{v} \cdot \nabla\mathbf{v}) = \mathbf{J} \times \mathbf{B} - v_{th}^2 \nabla\rho, \tag{2}$$

$$\nabla\Phi = \mathbf{v} \times \mathbf{B} - \eta\mathbf{J}, \tag{3}$$

and

$$\nabla \cdot \mathbf{J} = 0. \tag{4}$$

Here $v_{th} \equiv [k(T_i/m_i + T_e/m_e)]^{1/2}$ is the sound speed. Because of interest in low-pressure phenomena, we ignore motion on the time scale associated with Alfvén waves so that Maxwell's equations reduce to Eq. (4); this enables us to introduce a scalar potential Φ to represent the electric field occurring in Ohm's law (Eq. (3)). We ignore finite-gyration-radius effects and the Hall terms in Ohm's law, keeping only a scalar electrical resistivity η. We assume that thermal conductivity is high and that the temperature is constant in both space and time. A discussion of how this constraint could be relaxed was given in [11]. The model thus contains many essential features, including acoustic wave phenomena, Pfirsch–Schlüter enhancement of diffusion [14], and inertial flows.

In systems with closed toroidal magnetic surfaces this set of fluid equations possesses certain constraints. In particular Eqs. (3) and (4), with the conditions that Φ and $J_\parallel$ be single-valued on a magnetic surface, lead to [1]

$$\oint \mathbf{J} \cdot \mathbf{B}\, d\Sigma/|\nabla\Psi| = 0, \tag{5}$$

and

$$\oint \mathbf{J} \cdot \nabla\Psi \, d\Sigma / | \nabla\Psi | = 0, \tag{6}$$

where $d\Sigma$ is an element of surface area and Ψ is a surface label.

Because of the symmetry it is convenient to decompose the field into poloidal and toroidal components:

$$\mathbf{B} = \mathbf{B}_p + \mathbf{B}_T , \tag{7}$$

where

$$\mathbf{B}_p = \nabla\phi \times \nabla\Psi/2\pi, \tag{8}$$

$$\mathbf{B}_T = g(\Psi) \nabla\phi. \tag{9}$$

Here ϕ is the angle around the axis of symmetry and Ψ is the poloidal flux contained inside the magnetic surface it labels. Clearly $\nabla\phi = \mathbf{e}_\phi/X$ with $X \equiv R - r\cos\theta$ the distance out from the axis of symmetry (see Fig. 1). The function g is assumed to

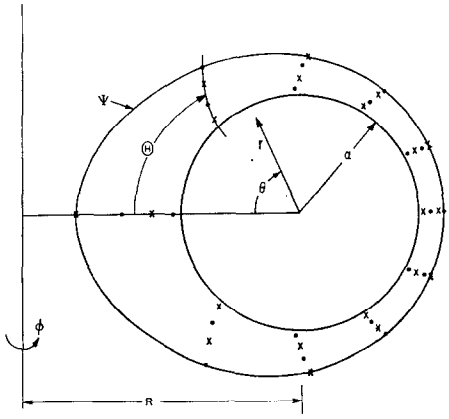

FIG. 1. Computational grid for model levitron of Eq. (11) with $B_0 = 3.3$ kG, $I_0 = 1.0$, $I_s = 0.25$, $B_v = -2.5$ kG, $R = 30$ cm, $r_0 = 10$ cm, $a = 5$ cm. The dots represent the main grid for ρ and v and the crosses label the main grid for Φ and J. Note that the mesh is constructed from surfaces of constant Ψ and Θ which do not coincide with the usually adopted cylindrical coordinates r and θ.

depend on Ψ alone, so that any currents associated with this imposed field lie on plasma surfaces. Thus, our field satisfies the equilibrium conditions for the plasma, and the model is valid only for electrostatic modes which do not provide serious field distortion.

In the past it has been expedient to work with an idealized model where $g = RB_0$ and

$$\Psi = 2\pi B_0 \int_0^r f(r)\, dr, \tag{10}$$

with B_0 a constant. Thus the magnetic surfaces labeled by Ψ have concentric circular cross sections and the poloidal field points only in the θ direction. Clearly, this magnetic field satisfies Maxwell's equations and the equilibrium condition only to the lowest order in an inverse aspect ratio expansion.

In this paper we adopt a model field for a levitron, generalized from that adopted by Kent and Stringer [15], which is accurate to first order in an inverse aspect ratio expansion. We again choose $g(\Psi) = RB_0 = I_0$, a constant that measures the total current along the axis of symmetry inside the plasma region. We choose as our flux surfaces:

$$\begin{aligned}\Psi = 2\pi R I_s\{&\ln(r/a) - (\cos\theta/2R)[(r-a)(2 + \ln(r/8R) - (2B_v R/I_s)) \\ &+ a\ln(r/a)] + \cdots\},\end{aligned} \tag{11}$$

with I_s the current carried by an inner ring of minor radius a and major radius R' and B_v the magnitude of a uniform vertical field. We find from Eq. (8) that with

$$\mathbf{B}_p = B_r \mathbf{e}_r + B_\theta \mathbf{e}_\theta, \tag{12}$$

$$B_r = -(I_s/2Rr)\sin\theta[(r-a)(2 + \ln(r/8R) - (2B_v R/I_s)) + a\ln(r/a) + \cdots],$$

and

$$B_\theta = (I_s/r)[1 - (r/2R)\cos\theta(1 + \ln(r/8R) - (2B_v R/I_s)) + \cdots].$$

Obviously one can determine $\Psi(r, \theta)$ numerically for any prescribed equilibrium distributions of $p(\psi)$ and $g(\psi)$ by solving the well-known equation for the stream function

$$\begin{aligned}\frac{1}{X}\left[\frac{\partial}{\partial X}\left(\frac{1}{X}\frac{\partial\Psi}{\partial X}\right) + \frac{1}{X}\frac{\partial^2\Psi}{\partial Z^2}\right] &= -\frac{2\pi J_\phi}{X} \\ &= -2\pi\frac{dp(\Psi)}{d\Psi} - \frac{\pi}{X^2}\frac{dg^2(\Psi)}{d\Psi}.\end{aligned} \tag{13}$$

III. Coordinate System

In this section we develop the geometry of the field line coordinates used in the numerical calculations. Our toroidal configuration is illustrated in Fig. 1. To construct an orthogonal Ψ, Θ, ϕ system we introduce a function Θ such that [16]

$$\mathscr{J} B_p^2 \nabla\Theta = \nabla\phi \times \nabla\Psi \tag{14}$$

with the Jacobian $\mathcal{J}(r, \theta)$ chosen so that Θ increases by 2π as θ is changed by 2π. For most applications it is necessary to solve Eq. (14) numerically in order to determine $r(\Psi, \Theta)$ and $\theta(\Psi, \Theta)$. For the usual idealized model [1] we obtain

$$\Theta = \theta, \qquad \mathcal{J}(r, \theta) = rX/B_0 f. \tag{15}$$

For the levitron model of Eq. (12), we find

$$\begin{aligned} \Theta &= \theta - (\sin\theta/2R)[r(1 + \ln(r/8R) - (2B_v R/I_s)) \\ &\quad - a \ln r\,(2 + \ln(a/8R) - (2B_v R/I_s)) + \cdots], \\ \mathcal{J} &= (r^2/I_s)\{1 + (\cos\theta/2R)[2r(1 + \ln(r/8R) - (2B_v R/I_s)) \\ &\quad - a \ln r\,(2 + \ln(a/8R) - (2B_v R/I_s)) + \cdots]\}. \end{aligned} \tag{16}$$

In this coordinate system the arc length is

$$dl^2 = (2\pi X B_p)^{-2}\, d\Psi^2 + (\mathcal{J} B_p)^2\, d\Theta^2 + X^2\, d\phi^2$$

so that the scale factors are given by

$$h_1 = (2\pi X B_p)^{-1}, \qquad h_2 = \mathcal{J} B_p, \qquad h_3 = X. \tag{17}$$

Differential operators such as gradient, divergence, and curl are thus easily evaluated.

We construct a uniform equally spaced grid in the (Ψ, Θ) plane with coordinates (Ψ_i, Θ_j) where

$$\begin{aligned} \Psi_i &= i\Psi_{\max}/N, \qquad 0 \leqslant i \leqslant N, \\ \Theta_j &= 2\pi j/M, \qquad 0 \leqslant j \leqslant M. \end{aligned}$$

A straightforward iteration scheme to solve Eqs. (10) and (15) or (11) and (16) for $r(\Psi_i, \Theta_j)$ and $\theta(\Psi_i, \Theta_j)$ so as to evaluate X, B_p, and the h_k's, has been found to converge satisfactorily.

The properties of the physical equations in the directions parallel and perpendicular to the magnetic field are considerably different. For this reason it is convenient to separate these equations into components in the $\nabla\Psi$, $\mathbf{B} \times \nabla\Psi$, and, $\mathbf{B}$ directions. Thus we introduce the unit vectors $\mathbf{e}_\Psi$, $\mathbf{e}_b$ and $\mathbf{e}_s \equiv \mathbf{e}_b \times \mathbf{e}_\Psi$, and decompose vectors in terms of them; for example

$$\mathbf{v} = v_\Psi \mathbf{e}_\Psi + v_s \mathbf{e}_s + v_b \mathbf{e}_b\,. \tag{18}$$

These are related to the base vectors $\mathbf{e}_\Psi$, $\mathbf{e}_\Theta$, $\mathbf{e}_\phi$ and thus $\mathbf{e}_r$, $\mathbf{e}_\theta$, $\mathbf{e}_\phi$ through

$$\mathbf{e}_\Psi = \mathbf{e}_\Psi\,, \qquad \mathbf{e}_\Theta = (B_T/B)\,\mathbf{e}_s + (B_p/B)\,\mathbf{e}_b\,, \qquad \mathbf{e}_\phi = -(B_p/B)\,\mathbf{e}_s + (B_T/B)\mathbf{e}_b\,.$$

IV. Numerical Methods and Finite-Difference Equations

Before considering the finite-difference equations we briefly summarize the solution procedure [1]. First $\mathbf{J}_\perp$ is obtained from Eq. (2), then J_b is determined from Eq. (4) (the constant of integration is adjusted so that Eq. (5) is satisfied). The parallel component of Ohm's law, Eq. (3), is used to obtain that part of the electrostatic potential $\hat{\Phi}$ which varies on a magnetic surface. The surface constant $\langle\Phi\rangle$ is advanced in time using the component of Ohm's law normal to a magnetic surface, the perpendicular component of momentum conservation lying in the surface, and the constraint for conservation of charge, Eq. (6). With the total potential $\Phi = \langle\Phi(\Psi)\rangle + \hat{\Phi}(\Psi, \Theta)$, the perpendicular components of Ohm's law give $\mathbf{v}_\perp$. Finally ρ and v_b are advanced in time using Eqs. (1) and (2).

From a numerical point of view the equations for the evaluation of the physical quantities fall into two categories: essentially time-independent equations from which $\mathbf{J}$, $\mathbf{v}_\perp$ and $\hat{\Phi}$ are evaluated, and time-dependent equations used to advance ρ, v_b, and $\langle\Phi\rangle$. In the first type we represent differential operators as closely as possible by space-centered differences; we use the Lax–Wendroff two-step numerical scheme [17] for the remaining equations.

At a given time step in the numerical calculation the various physical quantities are staggered over the mesh as illustrated in Fig. 1. This layout greatly helps the space and time centering of the various finite-difference equations. Thus the main grid (at integral multiples of Δt where the Lax–Wendroff scheme gives second-order accuracy) for ρ and $\mathbf{v}$ is represented by the dots while the main grid for Φ and $\mathbf{J}$ is labeled by the crosses. We commence with initial values of ρ, v_b and $\langle\Phi\rangle$ on the main grid. With approximate values for $\mathbf{v}_\perp$ (obtained from the previous step during the calculation under the assumption that $\partial\mathbf{v}_\perp/\partial t$ is small) the inertial terms are evaluated, again on the main grid. Then $\mathbf{J}$ and $\hat{\Phi}$ (and hence Φ) are evaluated on the auxiliary grid at the time t, and improved values of $\mathbf{v}_\perp$ obtained from Ohm's law. This sequence of steps is iterated until consistent values of $\mathbf{v}_\perp$ are obtained. In practice it is found that only one or two iterations are usually sufficient. The first step of the Lax–Wendroff method is then executed to give approximate values of ρ, v_b and $\langle\Phi\rangle$ on the auxiliary grid, appropriate to time $t + \Delta t/2$. The values of Φ, $\mathbf{J}$ and $\mathbf{v}_\perp$ on the auxiliary grid are then calculated in an identical fashion to that of the first step, and ρ, v_b and $\langle\Phi\rangle$ advanced to time $t + \Delta t$. Updating Φ, $\mathbf{J}$ and $\mathbf{v}_\perp$ on the main grid completes the advancement.

To improve the convergence of the iteration for $\mathbf{v}_\perp$, one can take advantage of the fact that part of v_s (depending on $\langle\Phi\rangle$) is known at the current time. Thus we take

$$v_s(\Psi_i, \Theta_j, n\,\Delta t) \equiv v^n_{s_{ij}} = v^{n-1}_{s_{ij}} - \bar{v}^{n-1}_{s_{ij}} + \bar{v}^n_{s_{ij}} \tag{19}$$

as a first approximation to v_s at time $n\,\Delta t$, where

$$\bar{v}_s \equiv (1/Bh_1)(d\langle\Phi\rangle/d\Psi). \tag{20}$$

The values of $\mathbf{J}_\perp$ are evaluated from Eq. (2). We find that

$$J^n_{\Psi_{ij}} = -(v^2_{th}B_T\delta_\Theta(\rho^n_{ij})/B + \mu_\Theta(\rho^n_{ij})\{\mu_\Theta(v^n_{\Psi_{ij}})\,\delta_\Psi(v^n_{s_{ij}}) + [B_T\mu_\Theta(v^n_{s_{ij}}) + B_p\mu_\Theta(v^n_{b_{ij}})]\,\delta_\Theta(v^n_{s_{ij}})/B + a^n_{s_{ij}} + \dot{v}^n_{s_{ij}}\})/B, \tag{21}$$

and

$$J^n_{s_{ij}} = (v^2_{th}\delta_\Psi(\rho^n_{ij}) + \mu_\Theta(\rho^n_{ij})\{\mu_\Theta(v^n_{\Psi_{ij}})\,\delta_\Psi(v^n_{\Psi_{ij}}) + [B_T\mu_\Theta(v^n_{s_{ij}}) + B_p\mu_\Theta(v^n_{b_{ij}})]\,\delta_\Theta(v^n_{\Psi_{ij}})/B + a^n_{\Psi_{ij}} + \dot{v}^n_{\Psi_{ij}}\})/B. \tag{22}$$

In these equations the vector **a** represents that part of the inertial term resulting from the curvature of the coordinate system. Thus

$$\begin{aligned} a_\Psi &= v_\Psi(v_\Psi(\partial h_1/\partial\Theta) - v_\Theta(\partial h_2/\partial\Psi))/h_1h_2 - v_\phi{}^2(\partial h_3/\partial\Psi)/h_1h_3\,,\\ a_s &= v_\Psi[B_T(v_\Theta(\partial h_2/\partial\Psi) - v_\Psi(\partial h_1/\partial\Theta))/h_2B - B_pv_\phi(\partial h_3/\partial\Psi)/h_3B]/h_1\\ &\quad - v_\phi v_b(\partial h_3/\partial\Theta)/h_2h_3\,, \end{aligned}$$

and

$$\begin{aligned} a_b &= v_\Psi[B_p(v_\Theta(\partial h_2/\partial\Psi) - v_\Psi(\partial h_1/\partial\Theta))/h_2B + B_Tv_\phi(\partial h_3/\partial\Psi)/h_3B]/h_1\\ &\quad + v_\phi v_s(\partial h_3/\partial\Theta)/h_2h_3\,. \end{aligned} \tag{23}$$

The centered difference and averaging operators are defined at the point Ψ_i, Θ_j and time n to be

$$\begin{aligned} \delta_\Psi(\rho^n_{ij}) &= (\rho^n_{i+1\,j} - \rho^n_{i-1\,j})/h_1\,\Delta\Psi,\\ \delta_\Theta(\rho^n_{ij}) &= (\rho^n_{i\,j+1} - \rho^n_{i\,j-1})/h_2\,\Delta\Theta,\\ \mu_\Theta(\rho^n_{ij}) &= (\rho^n_{i\,j+1} + \rho^n_{i\,j-1})/2. \end{aligned} \tag{24}$$

These finite-difference equations can be applied equally well to any internal grid point; in the first step of the Lax–Wendroff scheme they are used to find values of $\mathbf{J}_\perp$ on the auxiliary grid, while in the second step they give $\mathbf{J}_\perp$ on the main grid. In Eqs. (21) and (22) the dot over a quantity refers to a partial time derivative, which is approximated by its value at the time $(n-1)\,\Delta t$.

Integrating Eq. (4) over a magnetic surface we find

$$J^n_{b_{i\,j-1}} = J^{*\,n}_{b_{i\,j-1}} - BC_i{}^n/h_1h_3B_p\,, \tag{25}$$

where $J^{*n}_{b_{i\,j-1}}$ is evaluated from the centered-difference equation

$$(h_1h_3/B)_{i\,j-1}(B_TJ_s + B_pJ_b{}^*)^n_{i\,j-1} = (h_1h_3/B)_{i\,j-3}(B_TJ_s + B_pJ_b{}^*)^n_{i\,j-3} - h_1\delta_\Psi[(h_2h_3J_\Psi)^n_{i\,j-2}], \tag{26}$$

and $C_i{}^n$ is a constant of integration to be determined from the constraint, Eq. (5); using the trapezoidal rule, we find

$$C_i{}^n = \sum_j (J_b{}^*{}^n_{ij}h_2B/B_p)\Big/\sum_j (h_2B^2/h_1h_3B_p{}^2). \tag{27}$$

Here the summation refers to only those points on the surface corresponding to the particular grid on which J_b is being updated.

In an identical manner we integrate the parallel component of Ohm's law, Eq. (3); thus

$$\hat{\Phi}^n_{i\,j-1} = \hat{\Phi}^n_{i\,j-3} - \eta\,\Delta\Theta\,\mu_\Theta[(h_2BJ_b/B_p)^n_{i\,j-2}]. \tag{28}$$

The calculations necessary to evaluate the constant of integration in this step, $\langle\Phi\rangle^n_i$, have already been done (see Eq. (34)). With the total electrostatic potential determined, the perpendicular components of Ohm's law give

$$v_{\Psi^n_{ij}} = -B_T\delta_\Theta(\hat{\Phi}^n_{ij})/BB_p - \eta\mu_\Theta(J_{s^n_{ij}})/B, \tag{29}$$

and

$$v_{s^n_{ij}} = \delta_\Psi(\Phi^n_{ij})/B + \eta\mu_\Theta(J_{\Psi^n_{ij}})/B. \tag{30}$$

The finite-difference equations for advancing ρ and v_b are quite straightforward:

$$\rho^{n+k}_{ij} = \sigma\rho^n_{ij} + (1-\sigma)\,\mu_\Theta(\rho^{n+1/2}_{ij}) + (k\,\Delta t/h_1h_2h_3)(\delta_\Psi[(h_2h_3\rho)^{n+k-1/2}_{ij}] + \delta_\Theta[(h_1h_3\rho(B_Tv_s + B_pv_b)/B)^{n+k-1/2}_{ij}]), \tag{31}$$

and

$$\begin{aligned} v_{b^{n+k}_{ij}} = {} & \sigma v_{b^n_{ij}} + (1-\sigma)\,\mu_\Theta(v_{b^{n+1/2}_{ij}}) \\ & + k\,\Delta t(-v^2_{th}B_p\delta_\Theta(\rho^{n+k-1/2}_{ij})/B\mu_\Theta(\rho^{n+k-1/2}_{ij}) \\ & - \mu_\Theta(v_{\Psi^{n+k-1/2}_{ij}})\,\delta_\Psi(v_{b^{n+k-1/2}_{ij}}) \\ & - \mu_\Theta[((B_Tv_s + B_pv_b)/B)^{n+k-1/2}_{ij}]\,\delta_\Theta(v_{b^{n+k-1/2}_{ij}}) \\ & - \mu_\Theta(a_{b^{n+k-1/2}_{ij}})). \end{aligned} \tag{32}$$

The component a_b is defined in Eq. (23). In the first step of the Lax–Wendroff scheme, these equations refer to the auxiliary grid and we use $\sigma = 1$, $k = 1/2$. Values on the main grid (one complete time step ahead) are then obtained in the next step with $\sigma = 0$, $k = 1$.

The calculation of $d\langle\Phi\rangle/d\Psi$ is a little more involved. Using Eq. (2) to obtain $\mathbf{J}_\perp$ and inserting into Eq. (6) as in [1], we obtain an equation for $\partial^2\Phi/\partial\Psi\,\partial t$. Since $\partial(d\langle\Phi\rangle/d\Psi)/\partial t$ is constant on the surfaces and can be taken outside the integral sign, this can be used to advance $d\langle\Phi\rangle/\partial\Psi$ in the form

$$\left(\frac{\partial}{\partial t}[d\langle\Phi\rangle/d\Psi]\right)_i^{n+k} = \sum_j \rho_{ij}^n (v_{th}^2 h_2 \delta_\Theta (h_3 B_T/B^2)_{ij}$$
$$- h_2 h_3 \{[\eta\mu_\Theta(j_{\Psi_{ij}}^n) + \delta_\Psi(\dot{\hat{\Phi}}_{ij}^n)]/B + v_{\Psi_{ij}}^n \delta_\Psi[\mu_\Theta(v_{s_{ij}}^n)]$$
$$+ (B_T v_s + B_p v_b)_{ij}^n \delta_\Theta[\mu_\Theta(v_{s_{ij}}^n)]/B$$
$$+ a_{s_{ij}}^n\}/B)\Big/\sum_j \rho_{ij}^n h_2 h_3/B^2 h_1 . \tag{33}$$

Here the summation applies only to points on the auxiliary grid for half integral values of k and to those on the main grid otherwise. The partial derivatives j_Ψ and $\dot{\hat{\Phi}}$ are again approximated from the previous time step. With Eq. (33) we advance the gradient of $\langle\Phi\rangle$ normal to the magnetic surface using

$$(d\langle\Phi\rangle/d\Psi)_i^{n+k} = \sigma(d\langle\Phi\rangle/d\Psi)_i^n + (1 - \sigma)(d\langle\Phi\rangle/d\Psi)_i^{n+1/2}$$
$$+ k\,\Delta t[\partial(d\langle\Phi\rangle/d\Psi)/\partial t]. \tag{34}$$

It is straightforward and easy to change this scheme from a Lax–Wendroff method to other ones. As previously noted, in the time advancement of Eqs. (31)–(34), the Lax–Wendroff scheme is obtained if we set $\sigma = 1$, $k = 1/2$ for the first step and $\sigma = 0$, $k = 1$ for the second. The ordinary leap-frog scheme is achieved by setting $\sigma = 1$, $k = 1$. Other weightings could be equally well constructed.

A simplified linear stability analysis of this scheme has been done [18] using the idealized model of Eq. (10) in a limit where coupling between the different magnetic surfaces can be neglected. It supports the belief that these finite-difference equations utilizing the Lax–Wendroff scheme will provide a consistent and convergent representation of the physical model even for complicated geometries provided the Courant–Friedrichs–Lewy condition, that

$$(|\,B_p v_s + B_T v_b\,| + B_p v_{th})(\Delta t/h_2 B\,\Delta\Theta) < 1 \tag{35}$$

at every mesh point, is satisfied. This appears to be born out in practice.

V. Boundary and Initial Conditions

In order to complete the specification of the problem we must prescribe boundary conditions for most of the variables at the plasma boundaries as well as initial values for some of the variables.

We assume that the outer surface is perfectly conducting so that $\hat{\Phi}$, and thus v_Ψ, is zero at the boundary. Since plasma is transported to this surface by outward diffusion and convection, fixing the density on the boundary acts as a plasma sink and prevents buildup inside the wall. This model provides a crude representation of limiter behavior. The components of $\mathbf{v}$ in this surface may be allowed to free stream, or can be fixed throughout the run. In simulations of a levitron the electrostatic potential Φ is set equal to zero on the outside boundary and allowed to vary with time on the ring according to Eq. (34).

The initial conditions pose more of a problem. In principle, initial conditions are only required for those equations which are used explicitly to advance quantities in time. Thus we require initial distributions for ρ, v_b, and $d\langle\Phi\rangle/d\Psi$. Values of the other variables, $\mathbf{J}$, $\hat{\Phi}$, $\mathbf{v}_\perp$ are then obtained at the initial time from Eqs. (21)–(30).

Considered as a pure initial-value problem, there is some interest in following the time development from any given initial condition. On the other hand, the presence of large-amplitude oscillations may confuse the interpretation of the results and the accurate measurement of growth rates. Ideally one would like to be able to set up a near equilibrium solution with these amplitudes set to zero; individual physical effects can then be studied by perturbing the initial configuration in a well-prescribed manner. Short of finding an approximate analytical equilibrium [3], the best one can hope to do is to construct initial conditions numerically which are near steady state in the sense that during the first time step the force terms are small. The most convenient technique for achieving this involves iterating through the equations, systematically readjusting the variation of ρ and v_b over the magnetic surfaces, until the initial values of $\partial\rho/\partial t$ and $\partial v_b/\partial t$ are forced to zero. In this way we can hope to achieve initial conditions relatively free from acoustic and entropy modes. On the other hand, the complicated nature of the equation used to advance $\langle\Phi\rangle$ with time does not fit easily into this scheme, so that in practice the initial conditions always generate some geodesic oscillations [19].

Under these circumstances the most useful way of specifying the initial conditions is to prescribe average values for the density, parallel velocity and $d\langle\Phi\rangle/d\Psi$ on each surface. Appropriate equations for constructing a near steady state are easily derived. For the jth step in the iteration procedure we find by setting $\partial/\partial t = 0$ in the parallel component of the momentum equation,

$$\rho^{(j)} = \frac{1}{v_{th}^2}\int_0^\Theta \rho^{(j-1)}[\mathbf{v}^{(j-1)} \cdot \nabla\mathbf{v}^{(j-1)}]_b \frac{h_2}{B_p}\, d\Theta + \tilde{\rho}^{(j)} = \rho^* + \tilde{\rho}^{(j)}. \tag{36}$$

Specifying the total mass on a surface, we find

$$\bar{\rho}^{(j)} = -\oint (\rho^* - \rho_0)\, h_1 h_1 h_3\, d\Theta \Big/ \oint h_1 h_2 h_3\, d\Theta, \tag{37}$$

where $\rho_0(\Psi)$ is the prescribed constant value of density on the surface. Similarly, using particle conservation, we set

$$v_b^{(j)} = -\left(\frac{B_T}{B_p}\right) v_s^{(j-1)} - \left[\int_0^{\Theta} \frac{\partial}{\partial \Psi} (h_2 h_3 \rho^{(j-1)} v_\Psi^{(j-1)})\, d\Theta\right] \Big/ h_1 h_3 \rho B_p - \bar{v}_b^{(j)}/(h_1 h_3 \rho B_p). \tag{38}$$

Here $\bar{v}_b^{(j)}$ is determined by specifying the total toroidal momentum

$$\bar{v}_b^{(j)} = \frac{\oint [\rho^{(j)}(B_T v_b^* - B_p v_s^{(j-1)}) - \rho_0 v_0]\, h_2 h_3\, d\Theta / B B_p}{2\pi \oint B_T h_2 X\, d\Theta / B_p}. \tag{39}$$

These equations can be iterated numerically quite easily by solving alternative steps on the main and auxiliary grids and evaluating the various integrals with the trapezoidal rule. In practice the iteration is found to converge after only a few steps in most applications.

VI. Applications

The real value of a code of this nature is that it can be used for a variety of different numerical experiments. Here we concentrate on several aspects related to wave propagation and the nature of near steady-state flows in a levitron.

Measurement of the frequencies of characteristic oscillations in a confinement system is of considerable interest experimentally, especially as a diagnostic tool. Some analytic results have been obtained for low-pressure, static magnetic field toroidal systems as considered here. First, an eigenvalue equation whose solutions represent the normal modes of linear oscillation for a nondissipative system was obtained for a purely static equilibrium in a general axisymmetric confining magnetic field [19]. For a large aspect ratio device with concentric circular magnetic surfaces, the normal modes are quite easily shown to consist of pure $\sin\theta$ or $\cos\theta$ oscillations on a magnetic surface. More extensive analytic calculations including nonideal effects such as plasma inertia, resistivity and finite heat conduction have been carried out on this model [3].

One particularly useful feature of these analytic results arises from the fact that in the simple model oscillations at the geodesic frequency are driven only by density perturbations varying as $\sin\Theta$, while the $\cos\Theta$ normal modes are propagated along the magnetic surfaces at the reduced sound speed (the acoustic velocity

multiplied by the ratio of the poloidal to total magnetic field strengths). This provides a convenient check on the accuracy of the code; by perturbing the density on a magnetic surface according to

$$\rho(\Psi, \Theta) = \rho_0(\Psi)[1 + \alpha \sin(\Theta + \delta)], \tag{40}$$

one should be able to observe oscillations in the density at the geodesic frequency if $\delta = 0$ and at the acoustic frequency if $\delta = \pi/2$. For intermediate values of δ a more complicated mode coupling results. With $\delta = \pi/4$, this coupling is somewhat simplified, with acoustic oscillations being observable in the density at $\Theta = 0$ and geodesic oscillations at $\Theta = \pi/2$.

Typical results obtained with $\alpha = 0.01$ and $\delta = \pi/4$ are shown in Tables I and II. Here we use the model of Eq. (11) with parameters appropriate to a large aspect ratio device: major radius $R = 100$ cm, plasma radius $r_0 = 5$ cm and ring radius $a = 1$ cm, $B_0 = 12.5$ kG, with axial current $I_0 = 25$, ring current $I_s = 0.01$, and vertical field $B_v = 0$. We take $T = 25$ eV and assume classical resistivity. The initial conditions have zero flows and a parabolic density profile $\rho_0(\Psi)$, vanishing both at $r = a$ and $r = r_0$. We construct a grid with $N = 16$, $M = 16$ and use as time step $\Delta t = 0.2\,\mu$sec. In Tables I and II, we compare the computed acoustic and geodesic frequencies evaluated in a variety of ways with their analytic values, as given by the normal mode equation [19] on several different magnetic surfaces. One can see from the data that the code simulates the linear phase of the natural

TABLE I

Acoustic Frequency[a]

Surface radius (cm)	Computed frequency (kHz)		Analytic frequency (kHz)
	$\rho(\Theta = 0)$	$v_b(\Theta = \pi/2)$	
1.33	24.3	24.3	24.2
1.61	16.3	16.3	16.4
1.95	10.8	10.9	11.1
2.36	7.41	7.34	7.49
2.85	4.90	4.95	5.07
3.44	3.65	3.39	3.43

[a] Comparison of the computed acoustic frequencies and the corresponding analytic expression on several magnetic surfaces for a near circular small aspect ratio configuration. The computational results were obtained by following the time dependence of the density at $\Theta = 0$, and the parallel component of the fluid velocity at $\Theta = \pi/2$.

TABLE II
Geodesic Frequency[a]

Surface radius (cm)	Computed frequency (kHz)				Analytic frequency (kHz)
	$\langle v_\Theta \rangle$	$\langle v_\phi \rangle$	$\rho(\Theta = \pi/2)$	$v_b(\Theta = 0)$	
1.33	28.6	28.6	28.6	28.6	28.7
1.61	22.2	22.2	22.4	22.2	22.4
1.95	18.8	18.7	18.9	19.0	18.9
2.36	16.9	17.2	16.9	17.2	17.1
2.85	16.2	16.1	16.5	16.6	16.1
3.44	15.7	16.8	16.6	16.0	15.6

[a] Computed and analytic results for the geodesic frequency evaluated on several different magnetic surfaces as in Table I. The computed results were obtained from the time variation of the surface average of v_Θ, the surface average of v_ϕ, the density at $\Theta = \pi/2$ and the parallel component of velocity at $\Theta = 0$.

oscillations of the system in a quite satisfactory manner. We illustrate in Fig. 2 the time evolution of the parallel velocity component v_b at $\Theta = \pi/4$ on a surface near the inside of the plasma column ($r = 1.33$ cm). In this near circular geometry it can be well interpreted in terms of a simple beat pattern between two standing waves of equal strengths oscillating at the geodesic and acoustic frequencies, respectively. Over a longer period of time, however, this simple description is complicated by the buildup of the rotational instability [3] which couples the surfaces and the concomitant damping of the geodesic oscillations.

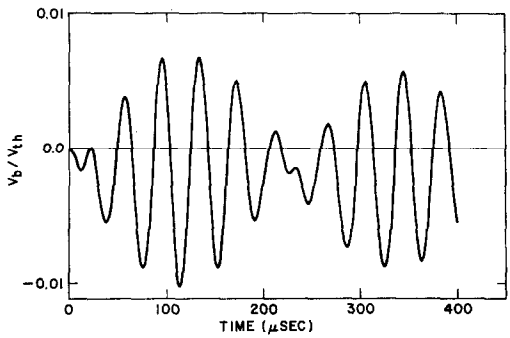

FIG. 2. Time evolution of the parallel velocity component v_b on an inner surface $r = 1.33$ cm at $\Theta = \pi/4$ in a large aspect ratio levitron with a nearly circular cross section; $B_0 = 12.5$ kG, $I_0 = 25.0$, $I_s = 0.01$, $B_v = 0.0$, $R = 100$ cm, $r_0 = 5$ cm, $a = 1$ cm. The beat pattern agrees well with the interaction of two standing waves of approximately equal strengths oscillating at the geodesic and acoustic frequencies, as determined in Tables I and II.

Next, we consider a system with a noncircular cross section typical of a laboratory spherator or levitron; we set $B_0 = 3.3$ kG, $I_0 = 1.0$, $I_s = 0.25$, $B_v = -2.5$ kG, $R = 30$ cm, $r_0 = 10$ cm, $a = 5$ cm, $T = 25$ eV, and $\eta =$ ten times classical resistivity. We use a grid with $N = 18$ and $M = 40$ and choose $\Delta t = 0.1\,\mu$ sec to satisfy the Courant–Friedrichs–Lewy stability criterion. A plot of typical magnetic surfaces for these parameters is shown in Fig. 1. We again assume an initial parabolic density profile in Ψ, iterating as described in Section V to obtain an initial state that is nearly free from acoustic waves. In Figs. 3–5 we follow the time evolution of $\rho(\Theta = 0)$, $v_b(\Theta = \pi/4)$, and the mean surface value of $v_\Theta = (B_T v_s + B_p v_b)/B$ on a surface near the center of the discharge. At early times these quantities show the presence of residual geodesic oscillations, which damp out as the rotational buildup occurs. The density evolution is controlled by resistive diffusion; evaluating the net plasma flow across a surface numerically we find excellent agreement (to three significant figures throughout the time of the simulation) with the analytic steady-state expression for Pfirsch–Schlüter diffusion in arbitrary geometries [14]. In Fig. 6 we show the flow patterns that develop in the system as the plasma moves along the field lines to compensate

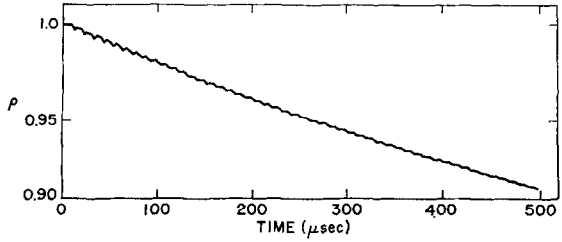

FIG. 3. Time evolution of the density on an inner surface $r \approx 6$ cm at $\Theta = 0$ in the configuration of Fig. 1. The oscillations occur at the geodesic frequency. The major feature is resistive decay.

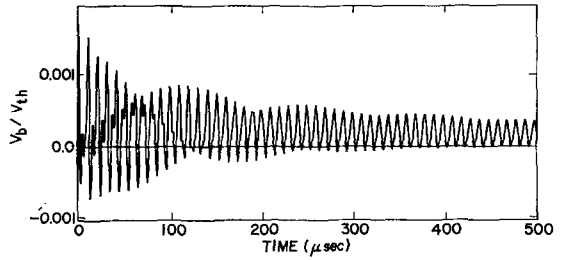

FIG. 4. Time evolution of the parallel velocity component v_b at $\Theta = \pi/4$ in the configuration of Fig. 3. As in Fig. 2 the beat pattern associated with the interaction of the geodesic and acoustic waves is evident at early times.

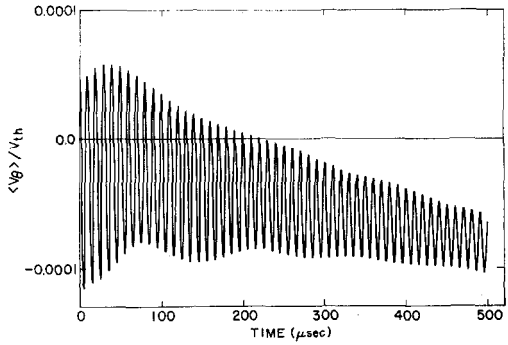

FIG. 5. Time evolution of the mean surface value of $v_\Theta = (B_T v_s + B_p v_b)/B$ in the configuration of Fig. 3.

for the drifts induced by field line curvature. Comparison with Fig. 6 of [3] shows that the hard core in a levitron introduces considerable complication.

To summarize, we have developed a fluid simulation that can follow the development of a plasma in a realistically shaped axisymmetric configuration such as a levitron for times of experimental interest. It is useful for studying wave propagation in a plasma, a subject that may provide new diagnostic techniques, and is useful for understanding plasma heating. We have used the code to study plasma diffusion

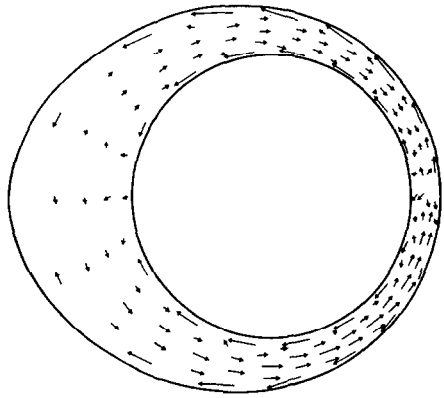

FIG. 6. Flow pattern that develops in the configuration of Fig. 1 as the plasma moves along the field lines to compensate for the drifts induced by field line curvature. The arrows indicate the projection of the flow onto a constant ϕ surface. The magnitude of the flow is represented by the length of the lines. Note that the plasma tends to flow outward in the center of the plasma and to return near the conducting wall and the inner ring. The major component of the flow is along the field lines.

in a realistic configuration over a long period of time and have shown that it is in good agreement with classical predictions (which are based on the asssumption of a static plasma) even when the magnitude of the plasma flow in the surface has built up to several percent of the sound speed. The model also provides a way of investigating the buildup of plasma flows.

ACKNOWLEDGMENTS

This work was initiated while both authors were at the UKAEA Culham Laboratory, and much of it was completed there. One of us (JLJ) must thank Drs. R. S. Pease and J. B. Taylor for their hospitality. We are indebted to Drs. K. E. Morton, T. E. Stringer, J. B. Connor, J. M. Greene, and B. McNamara for many useful discussions and valuable contributions. We are especially grateful to Dr. N. K. Winsor for his suggestions and critical comments. Part of this work was supported by US Atomic Energy Commission Contract AT(11-1)-3073, and use was made of computer facilities supported in part by National Science Foundation Grant NSF-GP579.

REFERENCES

1. N. K. WINSOR, J. L. JOHNSON, AND J. M. DAWSON, *J. Computational Phys.* **6** (1970), 430.
2. T. E. STRINGER, *Phys. Rev. Lett.* **22** (1969), 770.
3. J. M. GREENE, J. L. JOHNSON, K. E. WEIMER, AND N. K. WINSOR, *Phys. Fluids* **14** (1971), 1258.
4. E. BOWERS AND N. K. WINSOR, *Phys. Fluids* **14** (1971), 2203.
5. E. BOWERS AND N. K. WINSOR, "Proceedings of the IV Conference on Numerical Simulation of Plasmas," Naval Research Laboratory, Washington, DC, 1970, pp. 619.
6. J. M. GREENE AND N. K. WINSOR, *Phys. Fluids* **16** (1973), 863.
7. M. N. ROSENBLUTH AND J. B. TAYLOR, *Phys. Rev. Lett.* **23** (1969), 367.
8. T. E. STRINGER, *Phys. Fluids* **13** (1970), 1586.
9. A. A. GALEEV, *Zh.E.T.F. Pis Red* **10** (1969), 353 [*JETP Lett.* **10** (1970), 225].
10. O. P. POGUTSE, *Nucl. Fusion* **10** (1970), 399.
11. R. C. GRIMM AND J. L. JOHNSON, *Plasma Phys.* **14** (1972), 617.
12. M. A. HELLBERG, N. K. WINSOR, AND J. M. DAWSON, *Phys. Rev. Lett.* **28** (1972), 1022.
13. M. G. HAINES, *Phys. Rev. Lett.* **25** (1970), 1480.
14. J. L. JOHNSON AND S. VON GOELER, *Phys. Fluids* **12** (1969), 255.
15. A. KENT AND T. E. STRINGER, "Plasma Physics and Controlled Nuclear Fusion Research," International Atomic Energy Agency, Vienna, 1969, pp. 299.
16. I. B. BERNSTEIN, E. A. FRIEMAN, M. D. KRUSKAL, AND R. M. KULSRUD, *Proc. Roy. Soc.* **A 144** (1958), 17.
17. R. D. RICHTMYER AND K. W. MORTON, "Difference Methods for Initial-Value Problems," Interscience, New York, 1967.
18. R. C. GRIMM AND J. L. JOHNSON, *J. Computational Phys.* **11** (1973), 591.
19. N. K. WINSOR, J. L. JOHNSON, AND J. M. DAWSON, *Phys. Fluids* **11** (1968), 2448.